MATERIALS CHEMISTRY FRONTIERS

RESEARCH ARTICLE

View Article Online
View Journal | View Issue

Cite this: *Mater. Chem. Front.*, 2021, **5**, 6522

Simple glycerol-assisted and morphology controllable solvothermal synthesis of $CeVO_4$/$BiVO_4$ hierarchical hollow microspheres with enhanced photocatalytic activities†

Miao Wang, Yingying Guo, Zedong Wang, Huihui Cui, Tongming Sun* and Yanfeng Tang*

Received 25th May 2021,
Accepted 9th July 2021

DOI: 10.1039/d1qm00770j

rsc.li/frontiers-materials

$CeVO_4$ hierarchical hollow microspheres with various morphologies have been synthesized *via* a simple glycerol (Gl)-assisted solvothermal route. They are constructed using different morphological nanoscaled units (nanoflakes, nanorods and nanowires) by adjusting the solvent ratio of the system. The Gl and L-aspartic acid (L-Asp) molecules act as structure–directing agents, meaning the $CeVO_4$ hierarchical materials feature adjustable structural variations with 0D, 1D, and 2D structures. A possible formation mechanism is proposed based on the Gl content-dependent and time-dependent morphological evolution results. Under visible-light irradiation, the degradation results towards methylene blue (MB) indicate that the photocatalytic performance of the $CeVO_4$/$BiVO_4$ composites could be easily tuned by simply varying the Gl content ratio and the amount of $BiVO_4$ NPs. Compared with pristine $CeVO_4$, the photodegradation efficiency of the hierarchical nanowires-assembled $CeVO_4$/$BiVO_4$ hollow microspheres exhibit a two-fold increase after doping with 10% $BiVO_4$ and the degradation rate reached 97.8% in 30 min. Owing to the easy fabrication, our strategy may provide broad possibilities for the future development of other hollow micro/nanostructures that exhibit an efficient performance.

1. Introduction

As one of the lanthanide vanadates, cerium vanadate ($CeVO_4$) has attracted significant attention owing to its broad applications in supercapacitors, laser host and electrochromic materials, gas sensors and catalysts.[1–5] In particular, with a wide band gap energy of around 3 eV, $CeVO_4$ may offer a large number of opportunities for photocatalysis. Despite the significant progress that has been made in previous studies, the applications of $CeVO_4$ photocatalysts are still restricted by many factors, such as their small surface area, fast charge recombination and limited light absorption under visible light.[6–8] It is highly desirable to maximize the light absorption and efficiency of photocatalysis for practical applications. Therefore, significant efforts have been made to design and synthesize $CeVO_4$ semiconductors for highly-efficient photocatalytic activities. Consequently, various micro/nanosized $CeVO_4$ structures have been prepared (particles, rods, cube-like and microspheres).[9–12] As is well known, the photocatalytic efficiency of $CeVO_4$ is strongly reliant on the morphology and crystalline structure. However, to the best of our knowledge, hierarchical $CeVO_4$ hollow microspheres organized by nanowires have not been reported and the relationship between the morphology and photocatalytic properties needs to be investigated further.

Nowadays, the designing of efficient hybrid visible-light responsive photocatalysts for the removal of organic contaminants from water has been considered as a great option for solving environmental crises.[13–18] Among the visible-light-driven photocatalysts, the $BiVO_4$-supported nanocomposite has been widely investigated owing to its excellent chemical stability and suitable electronic band structure (2.4 eV).[19–21] On the other hand, owing to the superior characteristics (low density, large surface area, high permeability and countless active sites), the 3D hierarchical structures have received extensive attention owing to the excellent photocatalytic efficiency and adsorption performance towards organic contaminants.[22–25] In this research, we explored the preparation of $CeVO_4$ hierarchical hollow microspheres with various morphologies *via* a simple glycerol-assisted solvothermal route, in which glycerol (Gl) and L-aspartic acid (L-Asp) act as structure–directing agents. The influence of the Gl content and the reaction time on the morphology and crystalline structure of the products was examined. In addition, we proposed a possible growth mechanism of the hierarchical $CeVO_4$ hollow microspheres assembled from different building units. Furthermore, the

College of Chemistry and Chemical Engineering, Nantong University, Nantong 226019, P. R. China. E-mail: stm7314@ntu.edu.cn, tangyf@ntu.edu.cn

† Electronic supplementary information (ESI) available. See DOI: 10.1039/d1qm00770j

photocatalytic performance of the $CeVO_4$ and $CeVO_4/BiVO_4$ hierarchical hollow microspheres towards methylene blue (MB) was thoroughly investigated under visible-light irradiation. When the molar ratio of $CeVO_4$ and $BiVO_4$ was 1 : 0.1, the MB degradation rate reached 97.8% within 30 min.

2. Experimental section

2.1. Synthesis of hierarchical nanowires-assembled $CeVO_4$ hollow microspheres

All the regents used were of analytical grade. Typically, a mixture of $Ce(NO_3)_3{\cdot}6H_2O$ (1.0 mmol) and L-Asp (1.0 mmol) was dissolved in a solution of Gl (6 mL) and H_2O (18 mL), then 1.0 mmol NH_4VO_3 was added. After stirring vigorously for 20 min, the mixture was sealed in a 30 mL Teflon-lined stainless steel autoclave and heated at 150 °C for 24 h. After being cooled down to room temperature, the obtained precipitate was filtered, cleaned with distilled water and ethanol several times, and later dried at 80 °C for 3 h. Different morphological $CeVO_4$ micro/nanostructures were prepared by comparative experiments including different reaction times (3, 6 and 12 h) and different volume ratios of Gl/H_2O.

2.2. Synthesis of $CeVO_4/BiVO_4$ nanocomposites

A typical $CeVO_4/BiVO_4$ nanocomposite was prepared as follows: 1 mmol as-prepared $CeVO_4$ was dispersed in 24 mL deionized water with magnetic stirring. 0.1 mmol $Bi(NO_3)_3{\cdot}6H_2O$ and 1 mmol NH_4VO_3 were subsequently added to the mixture, then the solution was stirred for 20 min. The mixture was sealed in a 50 ml Teflon-lined stainless-steel autoclave, heated at 150 °C for 3 h, and then naturally cooled to room temperature. The resulting solution was centrifuged and cleaned with distilled water and ethanol several times, and later dried at 80 °C for 3 h to gain a yellow powder. The molar ratios of $CeVO_4$ and $BiVO_4$ were 1 : 0.3, 1 : 0.5, 1 : 0.7 and 1 : 1. As a comparison, pure $BiVO_4$ was prepared without the addition of $CeVO_4$.

2.3. Characterization

The crystalline phase and structure of the products were analyzed using X-ray diffractometry (XRD) on a Bruker D8-Advance powder X-ray diffractometer (Cu Kα radiation λ = 0.15418 nm). The surface morphologies of the $CeVO_4$ and $CeVO_4/BiVO_4$ were observed using scanning electron microscopy (SEM, Hitachi S-4800) and transmission electron microscopy (TEM, JEOL-2100F). The Brunauer–Emmett–Teller (BET) specific surface area was obtained from standard N_2 adsorption–desorption isotherms measured using Micromeritics ASAP 2020C apparatus. X-ray photoelectron spectroscopy (XPS) spectra were collected on a ESCALAB MK II X-ray photoelectron spectrometer using a nonmonochrome Mg K-X-ray as an excitation source. UV-vis diffuse-reflectance spectra (DRS) was recorded with a Shimadzu UV-3600 spectrometer. An EMX-10/12 electronic paramagnetic resonance (EPR) spectrometer with a Xe lamp (Heraeus fur Strahler Q180, Bruker) was used to record the EPR spectra.

2.4. Photocatalytic degradation of MB

The visible-light photocatalytic activity of the samples was determined by irradiating MB solution under a Xe lamp (100 W) with a 420 nm cutoff filter, which was conducted in an XPA-7 photochemical reactor. Before irradiation, 24 mg of the $CeVO_4$ sample was added into a series of quartz cuvettes containing 30 mL of MB solution (20 mg L^{-1}) and this mixture was magnetically stirred for 30 min in the dark to achieve an adsorption–desorption equilibrium between the sample and the MB molecules. During irradiation, the quartz cuvette was carefully taken from the reactor at the given time. 3.5 mL of the solution was taken out and centrifuged to separate the samples. The UV-Vis absorption spectrum was then recorded on a Shimadzu UV-3600 spectrophotometer.

3. Results and discussion

Fig. 1a shows the XRD patterns of an as-prepared typical sample. All diffraction peaks are in good agreement with the tetragonal phase of $CeVO_4$ (JCPDS No. 12-0757) and no impurities were detected. The strong diffraction peaks show that $CeVO_4$ are well-crystallized. Fig. 1b and c shows the SEM images of the typical $CeVO_4$. The low-magnification SEM image indicated that some

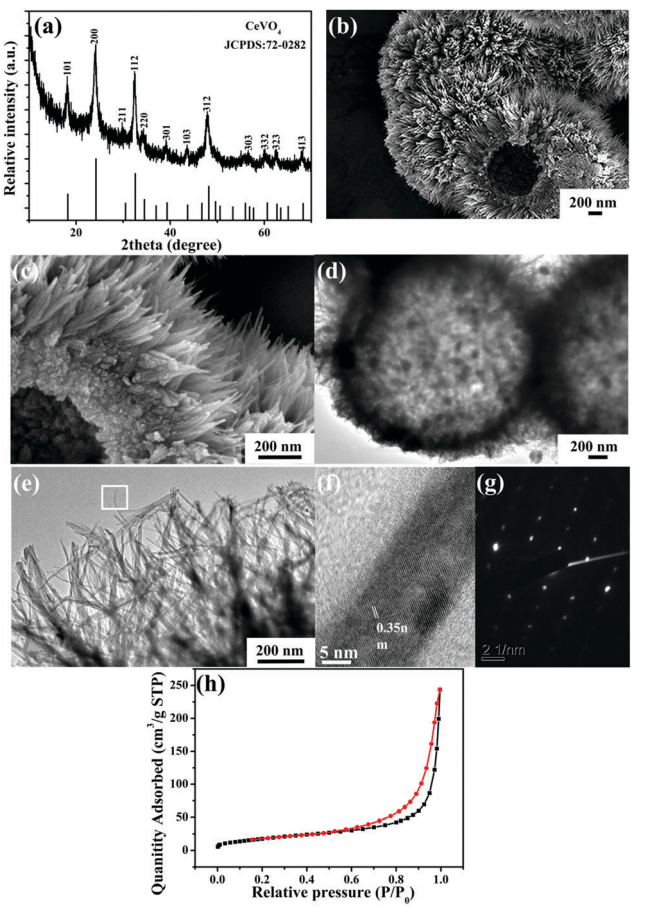

Fig. 1 XRD (a), SEM (b and c), TEM (d and e), HRTEM (f), SAED pattern (g) and N_2 adsorption–desorption isotherm (h) of a typical $CeVO_4$ sample.

hollow microspheres with an average diameter of about 2 μm were formed. The hollow interior and the shell outside are clearly observed in some broken spheres. The magnified SEM image from a single hollow sphere (Fig. 1c) reveals that it is self-assembled from a significant number of nanowires with an average length of about 400 nm. The hollow interiors of the $CeVO_4$ microspheres were also directly reconfirmed using the TEM images, as shown in Fig. 1d and e, an obvious contrast between the edges and the center can be observed under the electric beam, evidently confirming the hollow nature of the $CeVO_4$. The high magnification TEM image illustrates that the hollow microsphere is comprised of numerous nanowires, consistent with the SEM results. The high resolution transmission electron microscopy (HRTEM) image and the selected area electron diffraction (SAED) pattern (Fig. 1f and g) of a typical nanowire show that it is single-crystalline, and the spacing of approximately 0.35 nm between adjacent lattice planes corresponds to the distance between two (200) crystal planes. The BET specific surface area of the as-synthesized typical $CeVO_4$ hollow microspheres was investigated using N_2 adsorption–desorption measurements. As shown in Fig. 1h, the isotherm displays a typical H3 type hysteresis loop at a relative pressure (P/P_0) of between 0.6 and 1.0. The presence of hysteresis revealed the existence of hollow structures in the sample, which is in agreement with the observations from SEM and TEM. The BET surface area of the nanowires-assembled $CeVO_4$ hollow microspheres obtained using the typical procedure was 146.76 $m^2\ g^{-1}$.

The chemical composition and electronic state of the as-prepared samples were further measured using XPS measurements. Fig. 2a displays the XPS survey spectra of the as-prepared samples, indicating that there are only Ce, V, O and C elements. In the high-resolution Ce 3d spectra (Fig. 2b), two characteristic peaks of Ce $3d_{5/2}$ are observed at about 885.7 and 881.5 eV, and those representing Ce $3d_{3/2}$ are observed at about 904.1 and 900.3 eV, implying the existence of Ce^{3+} ions.[26] The V 2p spectra (Fig. 2c) of all samples are at approximately 516.9 eV (V $2p_{3/2}$) and 524.7 eV (V $2p_{1/2}$), ascribed to V^{5+}. The fitted result of the O 1s spectrum in Fig. 2d displays two binding energies at 529.8 and 531.5 eV, indicating contributions from the two species of lattice oxygen (O_2) in $CeVO_4$.[26,27]

To study the effects of the Gl content on the morphology and crystalline structure of the products, a series of contrast experiments were performed. Similar procedures were performed under the same reaction conditions, except for the use of different mixed solutions with Gl volumes of 0, 12, 18 and 24 mL instead of the previously used solution (6 mL Gl/18 mL H_2O). Fig. 3a shows the XRD patterns of the as-prepared $CeVO_4$ samples with various Gl dosages. All the diffraction peaks are indexed to pure tetragonal $CeVO_4$. With a decrease in the amount of added Gl, the diffraction peaks of the samples become sharper and the growth rate of the (200) lattice plane is faster than that of the other lattice planes, suggesting the introduction of water is beneficial to the crystallinity and growth of $CeVO_4$. The SEM images of the products obtained using different Gl contents are shown in Fig. 3b–f. There are many nanoflake-aggregated hollow microspheres in the absence of Gl (Fig. 3b), which is consistent with results reported in our previous work.[12] As shown in Fig. 3c–f, nanowires, nanorods and nanoparticles-assembled microspheres are obtained when 6 mL Gl, 12 mL Gl and 24 mL Gl are used, respectively. Comparatively, the dimensions of the nanowires are much larger than those obtained with larger amounts of Gl, suggesting the addition of GL is unfavorable to the nuclei and the growth of $CeVO_4$ nanostructures. Therefore, Gl molecules play a key role in the formation of $CeVO_4$ with different morphologies and crystallinities. In a typical procedure, a suitable dosage of the Gl molecule will increase the opportunity for the formation of one-dimensional $CeVO_4$ aggregated microspheres.

To better understand the formation process of the hierarchical structure, time-dependent experiments were conducted and the Gl volume was fixed as 8 mL. The intermediate products were measured using XRD and SEM analysis. As shown in Fig. 4a, the relative intensity of the samples is increased with an increase in the reaction time, revealing the crystallinity is improved. Detailed information on the corresponding microstructures is characterized and listed in Fig. 4b–f. After 3 h of reaction, many irregular tiny nanoparticles-assembled aggregates were prepared (Fig. 4b). After reacting for 6 h (Fig. 4c), the as-obtained nanoparticles

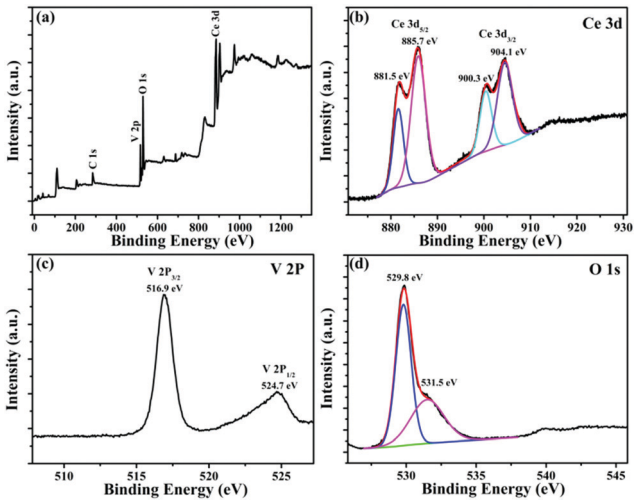

Fig. 2 XPS spectra for the as-obtained $CeVO_4$: (a) wide spectrum, (b) Ce 3d, (c) V 2p, and (d) O 1s.

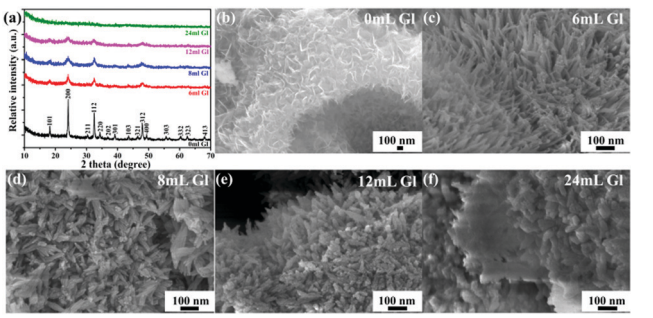

Fig. 3 XRD (a), and SEM images of the $CeVO_4$ samples obtained from different content of Gl: (b) 0 mL, (c) 6 mL, (d) 8 mL, (e) 12 mL, (f) 24 mL.

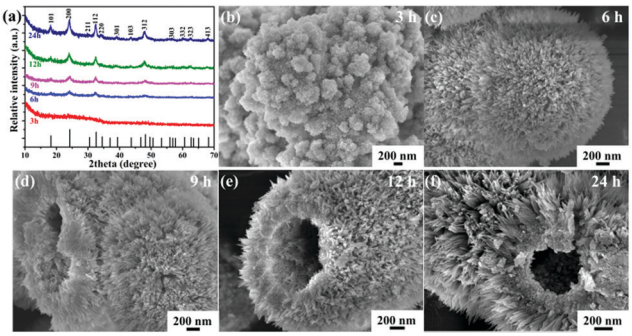

Fig. 4 XRD (a), and SEM images of the $CeVO_4$ samples obtained from different reaction times: (b) 3 h, (c) 6 h, (d) 9 h, (e) 12 h, (f) 24 h.

further grew into one-dimensional nanorods, thus nanorods-assembled hierarchical $CeVO_4$ microspheres were formed. With the reaction time increased from 9 to 24 h, as shown in Fig. 4d–f, the nanorods gradually evolved into nanowires, namely, the aspect ratio and particles sizes are larger than those of samples obtained within 3 h. Therefore, with the increasing reaction time, the as-obtained $CeVO_4$ samples undergo a morphological evolution from nanoparticles-assembled spheres to nanowires-assembled hierarchical hollow microspheres. These results indicate that the reaction time is a crucial factor in controlling the morphology of the products.

A possible formation mechanism was proposed based on the morphological evolution results, as shown in Fig. 5. Briefly, two key strategies are involved, namely, Gl content-dependent and time-dependent. With carboxyl and amino groups, the amino acid is a versatile, cheap and green complex agent and has been widely used as a morphology and structure directing agent in the nuclei, crystallization and aggregating process for inorganic nanomaterial synthesis.[12,28,29] Firstly, the VO^{3-} ions reacted with the Ce^{3+} ions to form $CeVO_4$. In distilled water (Step I), the initial $CeVO_4$ nanoparticles prefer to form 2D nanoflakes with the assistance of L-Asp and finally nanoflakes-assembled hollow microspheres are prepared, which have been reported in our previous work.[12] On the other hand, as a simple and potentially tridentate ligand, Gl molecules can effectively coordinate with rare-earth cations resulting in the formation of numerous complexes.[30] In the mixture of Gl and distilled water (step II), an extensive system of intermolecular hydrogen bonds between the OH–groups of the Gl kinetically control the anisotropic growth rates along the different crystal directions, which can lead to the formation of 1D micro/nanomaterials. Therefore, the formation of $CeVO_4$ with different morphologies results from the combined effects of L-Asp, water and Gl. Driven by the surface energy of the nanoparticles, $CeVO_4$ nanoparticles tend to grow along the 1D direction to form nanorods-assembled hollow microspheres and finally form nanowires-assembled hollow microspheres under suitable Gl conditions and longer reaction times, which are consistent with the Ostwald ripening (OR) mechanism.[31]

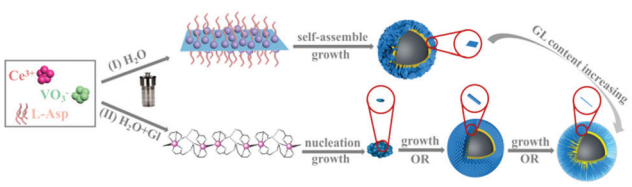

Fig. 5 Schematic illustration of the formation process of $CeVO_4$ hollow microspheres.

The XRD patterns of the typical $CeVO_4/BiVO_4$ composites (molar ratio as 1 : 0.1) are shown in Fig. 6a. There are coexisting diffraction peaks for both $CeVO_4$ and $BiVO_4$. The SEM image shown in Fig. 6b demonstrates the particles of $BiVO_4$ are well distributed on the surface of the $CeVO_4$ hollow microspheres. In addition, the elemental distribution of the sample was studied using TEM line mapping and elemental mapping images (Fig. S1, ESI†), proving that the elements Ce, V, O and Bi were homogeneously distributed through all the whole hollow microspheres. The energy band structure of a semiconductor is a crucial factor in determining its photocatalytic activity. The DRS spectra of the samples were measured. As shown in Fig. 6c, nanowires-assembled hollow microspheres of $CeVO_4$ have an obvious absorption in the region of 250–700 nm, as for pure $BiVO_4$, there is a broad absorption peak range from 200 to 500 nm. The band gaps of $CeVO_4$ and $BiVO_4$ are 1.00 and 2.06 eV (Fig. 6d), respectively, which are slightly lower than that of the previous reports.[26] Furthermore, the band gaps of the $CeVO_4/BiVO_4$ composites increase gradually with the addition of the $BiVO_4$, confirming the possible electronic transition between $CeVO_4$ and $BiVO_4$. Photoluminescence (PL) studies were performed to investigate the transfer and recombination process of the charge carriers in the samples. As presented in Fig. 6e, the broad emission peak centered at about 505 nm is ascribed to the radiative recombination process of self-trapped excitation. Compared with pure $CeVO_4$, $CeVO_4/BiVO_4$ heterostructures exhibited a weaker emission peak, showing that the recombination efficiency of the photoinduced carrier reduced, thereby giving a higher photocatalytic performance. Interestingly, the lowest PL intensity was obtained for the sample $CeVO_4/BiVO_4$ (1 : 0.1), revealing that the significantly

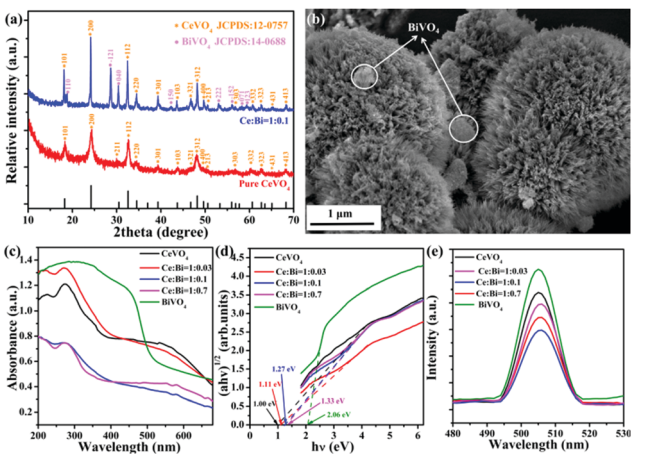

Fig. 6 (a) XRD patterns, (b) SEM image, (c) UV-vis DRS of the as-obtained samples, (d) the plots of $(\alpha h\nu)^{1/2}$ *versus* $h\nu$ and (e) PL of the typical $CeVO_4/BiVO_4$ composites (molar ratio as 1 : 0.1).

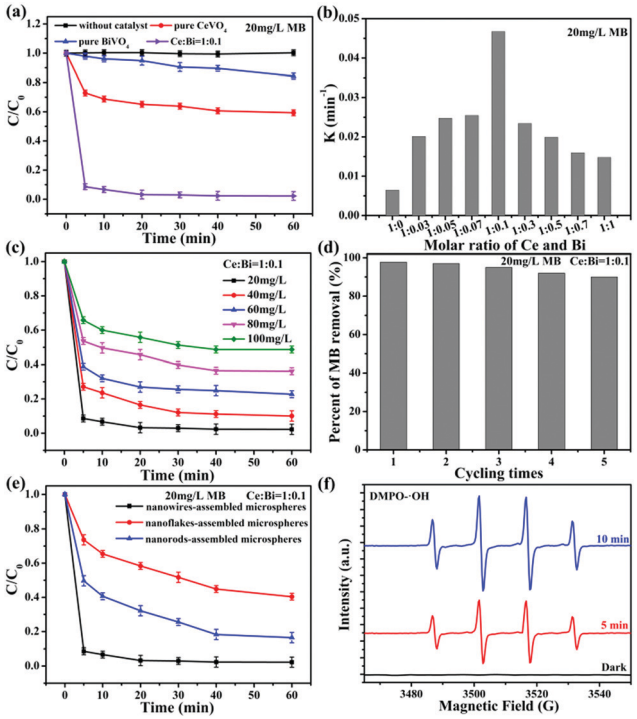

Fig. 7 Comparison of the photodegradation efficiency of MB on the $CeVO_4/BiVO_4$ catalysts: (a) different molar ratios; (b) photocatalytic kinetic reaction rate constant values; (c) different concentrations of MB; (d) recyclability; (e) different morphologies; and (f) ESR spectra of DMPO–•OH in a $CeVO_4/BiVO_4$ (1 : 0.1) sample.

weakened PL performance of $CeVO_4/BiVO_4$ was attributed to the synergistic effect of the electrons–holes transfer and $BiVO_4$ nanoparticles.

The photocatalytic activities of the samples were evaluated by measuring the decoloration of the MB solution under visible-light irradiation. By using the different molar ratios of $CeVO_4/BiVO_4$ composites as catalysts, Fig. 7a presents the degradation efficiency of MB (C/C_0) as a function of the irradiation time. Without any photocatalyst or in the presence of pristine $CeVO_4$, the degradation of MB was very slow under visible-light irradiation. Moreover, $BiVO_4$ had a significant effect on the photocatalytic process. Employing a 20 mg L^{-1} MB solution as a model pollutant, when $CeVO_4/BiVO_4$ (1 : 0.1) composites are introduced, the MB degradation reaches 97.8% within 30 min, which is higher than the other previously reported photocatalysts (Table 1). In addition, compared with pristine $CeVO_4$, the photodegradation efficiency of $CeVO_4/BiVO_4$ demonstrated a two-fold increase after doping with 10% $BiVO_4$. As the $BiVO_4$ content increases or decreases, the photocatalytic efficiency of the $CeVO_4/BiVO_4$ composites declined gradually (Fig. S2, ESI†), suggesting it follows the pseudo-first-order kinetic equation. Furthermore, the velocity constant value of $CeVO_4/BiVO_4$ (1 : 0.1) is 4.67×10^{-2} min^{-1}, which is higher than that of the other molar ratio (Fig. 7b).[35–37] Using fixed $CeVO_4/BiVO_4$ (1 : 0.1) as a typical catalyst, the photocatalytic degradation at different concentrations of MB was also investigated. Obviously, the higher the concentration of the MB solution, the lower the degradation rate (Fig. 7c). Fig. 7d shows the $CeVO_4/BiVO_4$ (1 : 0.1) photocatalytic recyclability towards the degradation of MB. The results indicated that $CeVO_4/BiVO_4$ (1 : 0.1) maintained its high MB degradation efficiency for up to five cycles. As shown in Fig. S3 (ESI†), the SEM and TEM images of the recovered samples show that the morphology of $CeVO_4/BiVO_4$ remains the same, suggesting the photocatalysts are of excellent chemical stability. On the other hand, the photocatalytic activities of other different morphological $CeVO_4/BiVO_4$ (1 : 0.1) micro/nano-structures were also assessed (Fig. 7e). Compared with nanorods or nanoflakes-assembled $CeVO_4/BiVO_4$ hollow microspheres, nanowires-assembled $CeVO_4/BiVO_4$ porous microspheres exhibited the best efficiency, implying the unique hollow microspheres had an excellent photocatalytic activity under visible-light irradiation. Therefore, the photocatalytic performance of the $CeVO_4/BiVO_4$ composites can be easily modulated by simply changing the morphologies of the $CeVO_4$ building units. As known, many factors including the size, crystallinity, morphology and BET surface area of the nanomaterials are key factors in achieving excellent photocatalytic performances. In this work, benefiting from the synergistic effects of the larger BET surface area, narrower energy gap, unique hierarchical structures and $BiVO_4$ doping, the nanowires-assembled $CeVO_4/BiVO_4$ hollow microspheres achieved a significantly improved photocatalytic efficiency.

Based on the above analysis, a schematic illustration for the photodegradation of MB by $CeVO_4/BiVO_4$ is proposed, as shown in Fig. 8. When exposed to light irradiation, $CeVO_4$ and $BiVO_4$ can be activated and produce electrons and holes. For $BiVO_4$, the electrons in the valence band (VB) are excited to the conduction band (CB) by leaving a hole on the VB. However, for $CeVO_4$, only part of the photoinduced electrons migrate from the VB to the CB. The photoinduced electrons on the CB of the $CeVO_4$ flow to that of the $BiVO_4$ and, in contrast, the holes on the VB of $BiVO_4$ migrate to that of the $CeVO_4$. The CB potential of the $CeVO_4$ semiconductor (0.415 eV) is more positive than the standard reduction potential of $O_2/{}^{\bullet}O^{2-}$ (−0.046 eV).[38] Thus, the

Table 1 Comparison of MB degradation efficiency on $CeVO_4/BiVO_4$ hollow microspheres with other reported catalysts

Materials	Light irradiation	Amount of catalyst (mg)	Degradable compounds	Removal percentage
Z-scheme $CeO_2/CeVO_4/V_2O_5$[8]	300 W Xe lamp	10	100 mL 10 mg L^{-1} MB	93.53% (240 min)
P-doped $CeVO_4$ nanorods[10]	300 W Xe lamp	50	50 mL 20 mg L^{-1} MB	100% (180 min)
Hedgehog-like $CeVO_4$–$BiVO_4$[26]	150 W Xe lamp	50	100 mL 50 mg L^{-1} levofloxacin	95.7% (300 min)
3% Dy doped $CeVO_4$ nanorods[32]	UV light Irradiation	200	200 mL 1 mol L^{-1} MB	94% (80 min)
$La_2O_3/CeVO_4$@halloysite nanotubes[33]	300 W Xe lamp	80	100 mL 20 mg L^{-1} tetracycline	61.9% (60 min)
$InVO_4/CeVO_4$ hollow nanobelts[34]	800 W Xe lamp	40	40 mL 20 mg L^{-1} tetracycline	92.4% (90 min)
$CeVO_4/BiVO_4$ microspheres	**100 W Xe lamp**	**24**	**30 mL 20 mg L^{-1} MB**	**97.8% (30 min)**

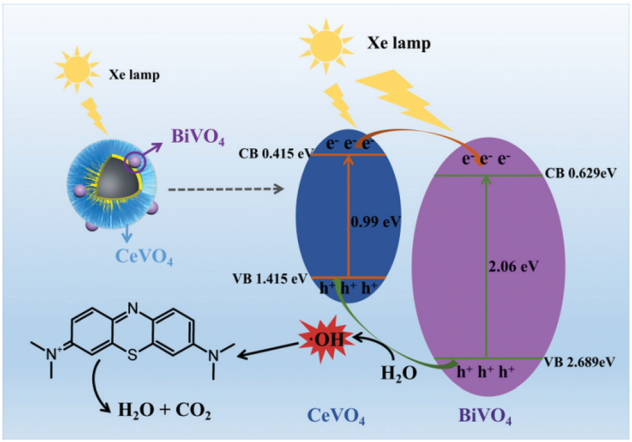

Fig. 8 Schematic illustration of MB degradation with $CeVO_4/BiVO_4$ composites under visible-light irradiation.

electrons of CB on the $CeVO_4$ surface cannot deoxidize O_2 into $^{\bullet}O^{2-}$. The VB potential of the $BiVO_4$ semiconductor (2.689 eV) is more positive than that of $^{\bullet}OH/H_2O$ (2.27 eV).[39] Thus, the photogenerated holes in the $BiVO_4$ directly oxidize MB and react with the surface adsorbed OH^- group forming $^{\bullet}OH$ radicals to oxidize the organic pollutants. To further confirm the existence of the active species $^{\bullet}OH$ in the photodegradation process, the electron paramagnetic resonance (EPR) of $CeVO_4/BiVO_4$ was conducted (Fig. 7f). It can be seen that the characteristic signal of $^{\bullet}OH$ is detected under visible light irradiation, and no signal is found in the dark. Meanwhile, the intensities of the characteristic signals are enhanced with the increasing irradiation time from 5 to 10 min, showing $^{\bullet}OH$ has a primary effect on improving the degradation of MB, which is consistent with the previously reported literature.

4. Conclusions

Employing Gl and L-Asp as morphology-directing agents, a simple solvothermal method was developed to prepare $CeVO_4$ hierarchical hollow microspheres assembled using different building units (nanowires, nanorods, nanoflakes and nanoparticles). Benefiting from the synergistic effects of the unique hierarchical hollow microspheres and $BiVO_4$ doping, nanowires-assembled $CeVO_4/BiVO_4$ heterostructures have achieved a significantly improved photocatalytic efficiency towards MB under visible-light irradiation. The content ratio of Gl/H_2O and the reaction time play crucial roles in the formation of products with different morphologies. The photocatalytic performance of the $CeVO_4/BiVO_4$ composites can be easily modulated by simply changing the morphologies of $CeVO_4$, and the photodegradation of MB demonstrates a two-fold increase after doping with 10% $BiVO_4$. Therefore, this simple Gl-assisted and morphology-controllable solvothermal route will provide an effective strategy for designing other hollow micro/nanostructures and the obtained hierarchical $CeVO_4/BiVO_4$ hollow microspheres are promising candidates for use in the photocatalytic field.

Conflicts of interest

There are no conflicts to declare.

Acknowledgements

This work was supported by the National Natural Science Foundation of China (No. 22075152, 21776140, 22073052) and the Science and Technology Projects Fund of Nantong City (JC2020134, JC2020133). We are very grateful to the Nantong University Analytical Testing Center for its support for testing.

References

1 J. Z. He, J. H. Zhao, Z. Run, M. J. Sun and H. Pang, Ultrathin cerium orthovanadate nanobelts for high-performance flexible all-solid-state asymmetric supercapacitors, *Chem. – Asian J.*, 2015, **10**, 338–343.
2 M. Y. Chang, M. F. Wang, Y. Q. Chen, M. M. Shu, Y. J. Zhao, B. B. Ding, Z. Y. Hou and J. Lin, Self-assembled $CeVO_4$/Ag nanohybrid as photoconversion agents with enhanced solar-driven photocatalysis and NIR-responsive photothermal/photody-namic synergistic therapy performance, *Nanoscale*, 2019, **11**, 10129.
3 J. M. Hou, H. H. Huang, Z. Z. Han and H. B. Pan, A role of oxygen adsorption and gas sensing mechanism for cerium vanadate ($CeVO_4$) nanorods, *RSC Adv.*, 2016, **6**, 14522–14558.
4 C. Wang, B. Yang, J. L. Xu, F. Xia and J. Z. Xiao, Effects of $CeVO_4$ electrode morphology and oxygen content on ammonia sensing properties for potentiometric sensor, *Sens. Actuators, B*, 2019, **299**, 126863.
5 T. Kokulnathan, T. S. Priya and T. J. Wang, Surface engineering three-dimensional flowerlike cerium vanadate nanostructures used as electrocatalysts: real time monitoring of clioquinol in biological samples, *ACS Sustainable Chem. Eng.*, 2019, **7**, 16121–16130.
6 M. Wang, X. M. Hu, Z. Y. Zhan, T. M. Sun and Y. F. Tang, Facile fabrication of $CeVO_4$ hierarchical hollow microspheres with enhanced photocatalytic activity, *Mater. Lett.*, 2019, **253**, 259–262.
7 P. Babu, S. Mohanty, B. Naik and K. Parida, Serendipitous assembly of mixed phase $BiVO_4$ on B-doped g-C_3N_4: an appropriate p–n heterojunction for photocatalytic O_2 evolution and Cr(VI) reduction, *Inorg. Chem.*, 2019, **58**, 12480–12491.
8 X. Cui, Z. Y. Liu, G. S. Li, M. Zhang, Y. T. Song and J. Wang, Self-generating $CeVO_4$ as conductive channel within CeO_2/$CeVO_4/V_2O_5$ to induce *Z*-scheme charge-transfer driven photocatalytic degradation coupled with hydrogen production, *Int. J. Hydrogen Energy*, 2019, **44**, 23921–23935.
9 K. Ye, X. H. Niu, H. W. Song, L. J. Wang and Y. X. Peng, Combining $CeVO_4$ oxidase-mimetic catalysis with hexametaphosphate ion induced electrostatic aggregation for photometric sensing of alkaline phosphatase activity, *Anal. Chim. Acta*, 2020, **1126**, 16–23.
10 Z. D. Liu, K. Sun, M. Z. Wei and Z. Ma, Phosphorus-doped cerium vanadate nanorods with enhanced photocatalytic activity, *J. Colloid Interface Sci.*, 2018, **531**, 618–627.

11 Y. Q. Shen, Y. C. Huang, S. J. Zheng, X. F. Guo, Z. X. Chen, L. M. Peng and W. P. Ding, Nanocrystals of $CeVO_4$ doped by metallic heteroions, *Inorg. Chem.*, 2011, **50**, 6189–6194.

12 J. J. Ding, X. Liu, M. Wang, Q. Liu, T. M. Sun, G. Q. Jiang and Y. F. Tang, Controlled synthesis of $CeVO_4$ hierarchical hollow microspheres with tunable hollowness and their efficient photocatalytic activity, *CrystEngComm*, 2018, **20**, 4499–4505.

13 M. Moniruddin, E. Oppong, D. Stewart, C. McCleese, A. Roy, J. Warzywoda and N. Nuraje, Designing CdS-based ternary heterostructures consisting of Cometal and CoOx cocatalysts for photocatalytic H_2 evolution under visible light, *Inorg. Chem.*, 2019, **58**, 12325–12333.

14 Y. R. Lv, R. Huo, S. Y. Yang, Y. Q. Liu, X. J. Li and Y. H. Xu, Self-assembled synthesis of PbS quantum dots supported on polydopamine encapsulated $BiVO_4$ for enhanced visible-light-driven photocatalysis, *Sep. Purif. Technol.*, 2018, **197**, 281–288.

15 T. K. Jia, F. Fua, J. L. Li, Z. Deng, F. Long, D. S. Yu, Q. Cui and W. M. Wang, Rational construction of direct *Z*-scheme SnS/g-C_3N_4 hybrid photocatalyst for significant enhancement of visible-light photocatalytic activity, *Appl. Surf. Sci.*, 2020, **499**, 143941.

16 X. L. Zhu, P. Wang, M. M. Li, Q. Q. Zhang, E. A. Rozhkova, X. Y. Qin, X. Y. Zhang, Y. Dai, Z. Y. Wang and B. B. Huang, Novel high-efficiency visible-light responsive $Ag_4(GeO_4)$ photocatalyst, *Catal. Sci. Technol.*, 2017, **7**, 2318–2324.

17 S. Mohanty, P. Babu, K. Parida and B. Naik, Surface-plasmon-resonance-induced photocatalysis by core–shell SiO_2@Ag NCs@Ag_3PO_4 toward water-splitting and phenol oxidation reactions, *Inorg. Chem.*, 2019, **58**, 9643–9654.

18 P. Babu, S. Mohanty, B. A. Naik and K. Parida, Synergistic effects of boron and sulfur codoping into graphitic carbon nitride framework for enhanced photocatalytic activity in visible light driven hydrogen generation, *ACS Appl. Energy Mater.*, 2018, **1**, 5936–5947.

19 M. Ganeshbabu, N. Kannan, P. S. Venkatesh, G. Paulraj, K. Jeganathan and D. MubarakAli, Synthesis and characterization of $BiVO_4$ nanoparticles for environmental applications, *RSC Adv.*, 2020, **10**, 18315–18322.

20 P. Babu, S. Mohanty, B. Naik and K. Parida, Serendipitous assembly of mixed phase $BiVO_4$ on B-Doped g-C_3N_4: an appropriate p–n heterojunction for photocatalytic O_2 evolution and Cr(VI) reduction, *Inorg. Chem.*, 2019, **58**, 12480–12491.

21 N. A. Mohamed, J. Safaei, A. F. Ismail, M. N. Khalid, M. F. Jailani, M. F. Noh, N. A. Arzaee, D. Zhou, J. S. Sagu and M. A. Teridi, Boosting photocatalytic activities of $BiVO_4$ by creation of g-C_3N_4/ZnO@$BiVO_4$ heterojunction, *Mater. Res. Bull.*, 2020, **125**, 110779.

22 M. Wang, T. M. Sun, Y. J. Shi, G. Q. Jiang and Y. F. Tang, 3D hierarchical ZnOHF nanostructures: synthesis, characterization and photocatalytic properties, *CrystEngComm*, 2014, **16**, 10624–10630.

23 H. Salari and H. Yaghmaei, *Z*-Scheme 3D Bi_2WO_6/MnO_2 heterojunction for increased photoinduced charge separation and enhanced photocatalytic activity, *Appl. Surf. Sci.*, 2020, **532**, 147413.

24 J. L. Zhou, M. Wu, Y. J. Zhang, C. G. Zhu, Y. W. Fang, Y. F. Li and L. Yu, 3D hierarchical structures MnO_2/C: a highly efficient catalyst for purification of volatile organic compounds with visible light irradiation, *Appl. Surf. Sci.*, 2018, **447**, 191–199.

25 Y. Y. Guo, Y. X. Mo, H. H. Cui, M. Wang, Y. F. Tang and T. M. Sun, Green and facile synthesis of hierarchical ZnOHF microspheres for rapid and selective adsorption of cationic dyes, *J. Mol. Liq.*, 2021, **329**, 115529.

26 G. Lu, Z. S. Lun, H. Y. Liang, H. Wang, Z. Li and W. Ma, *In situ* fabrication of $BiVO_4$–$CeVO_4$ heterojunction for excellent visible light photocatalytic degradation of levofloxacin, *J. Alloys Compd.*, 2019, **772**, 122–131.

27 I. Othman, J. H. Zain, M. A. Haija and F. Banat, Catalytic activation of peroxymonosulfate using $CeVO_4$ for phenol degradation: an insight into the reaction pathway, *Appl. Catal., B*, 2020, **266**, 118601.

28 T. A. King, J. M. Kandemir, S. J. Walsh and D. R. Spring, Photocatalytic methods for amino acid modification, *Chem. Soc. Rev.*, 2021, **50**, 39–57.

29 Y. X. Guo, S. W. Lin, X. Li and Y. P. Liu, Amino acids assisted hydrothermal synthesis of hierarchically structured ZnO with enhanced photocatalytic activities, *Appl. Surf. Sci.*, 2016, **384**, 83–91.

30 N. G. Naumov, M. S. Tarasenko, A. V. Virovets, Y. Kim, S. J. Kim and V. E. Fedorov, Glycerol as ligand: the synthesis, crystal structure, and properties of compounds $[Ln_2(H_2L)_2(H_3L)_4]$-$[Re_6Q_8(CN)_6]$, Ln = La, Nd, Gd, Q = S, Se, *Eur. J. Inorg. Chem.*, 2006, 298–303.

31 H. W. Liu and J. M. Chang, $CeVO_4$ yolk–shell microspheres constructed by nanosheets with enhanced lithium storage performances, *J. Alloys Compd.*, 2020, **849**, 156682.

32 A. Phuruangrat, T. Thongtem and S. Thongtem, Hydrothermal synthesis and characterization of Dy-doped $CeVO_4$ nanorods used for photodegradation of methylene blue and rhodamine B, *J. Rare Earths*, 2020, DOI: 10.1016/j.jre.2020.11.005.

33 J. R. Guan, J. Z. Li, Z. F. Ye, D. Y. Wu, C. Y. Liu, H. Q. Wang, C. C. Ma, P. W. Huo and Y. S. Yan, La_2O_3 media enhanced electrons transfer for improved $CeVO_4$@halloysite nanotubes photocatalytic activity for removing tetracycline, *J. Taiwan Inst. Chem. Eng.*, 2019, **96**, 281–298.

34 W. C. Ding, X. Lin, G. H. Ma and Q. F. Lu, Designed formation of $InVO_4$/$CeVO_4$ hollow nanobelts with *Z*-scheme charge transfer: synergistically boosting visible-light-driven photocatalytic degradation of tetracycline, *J. Environ. Chem. Eng.*, 2020, **8**, 104588.

35 X. B. Li, S. W. Yang, J. Sun, P. He, X. G. Xu and G. Q. Ding, Tungsten oxide nanowire-reduced graphene oxide aerogel for high-efficiency visible light photocatalysis, *Carbon*, 2014, **78**, 38–48.

36 P. Babu and B. Naik, Cu–Ag bimetal alloy decorated SiO_2@TiO_2 hybrid photocatalyst for enhanced H_2 evolution and phenol oxidation under visible light, *Inorg. Chem.*, 2020, **59**, 10824–10834.

37 S. W. Yang, C. C. Ye, X. Song, L. He and F. Liao, Theoretical calculation based synthesis of a poly(*p*-phenylenediamine)–Fe_3O_4 composite: a magnetically recyclable photocatalyst with high selectivity for acid dyes, *RSC Adv.*, 2014, **4**, 54810.
38 N. Li, Z. T. Liu, M. Liu, C. R. Xue, Q. Chang, H. Q. Wang, Y. Li, Z. C. Song and S. L. Hu, Facile synthesis of carbon dots@2D MoS_2 heterostructure with enhanced photocatalytic properties, *Inorg. Chem.*, 2019, **58**, 5746–5752.
39 G. Lu, F. Wang and X. J. Zou, Hydrothermal synthesis of *m*-$BiVO_4$ and *m*-$BiVO_4$/BiOBr with various facets and morphologies and their photocatalytic performance under visible light, *J. Alloys Compd.*, 2017, **697**, 417–426.